Isolating the two room-temperature polymorphs of NaNbO3 : structural features, optical band gap, and reactivity

Guillaume Gouget, Mathieu Duttine, Etienne Durand, Antoine Villesuzanne, Vincent Rodriguez, Frédéric Adamietz, Thierry Le Mercier, Marc-David Braida, Alain Demourgues

▶ **To cite this version:**

Guillaume Gouget, Mathieu Duttine, Etienne Durand, Antoine Villesuzanne, Vincent Rodriguez, et al.. Isolating the two room-temperature polymorphs of NaNbO3 : structural features, optical band gap, and reactivity. ACS Applied Electronic Materials, 2019, 1 (4), pp.513-522. 10.1021/acsaelm.8b00125 . hal-02121234

HAL Id: hal-02121234
https://hal.science/hal-02121234

Submitted on 6 May 2019

HAL is a multi-disciplinary open access archive for the deposit and dissemination of scientific research documents, whether they are published or not. The documents may come from teaching and research institutions in France or abroad, or from public or private research centers.

L'archive ouverte pluridisciplinaire **HAL**, est destinée au dépôt et à la diffusion de documents scientifiques de niveau recherche, publiés ou non, émanant des établissements d'enseignement et de recherche français ou étrangers, des laboratoires publics ou privés.

Isolating the two room-temperature polymorphs of $NaNbO_3$: structural features, optical band gap and reactivity

Guillaume Gouget,[a,†,*] Mathieu Duttine,[a] Etienne Durand,[a] Antoine Villesuzanne,[a] Vincent Rodriguez,[b] Frédéric Adamietz,[b] Thierry Le Mercier,[c] Marc-David Braida[c] and Alain Demourgues[a,*]

[a] CNRS, Université de Bordeaux, ICMCB, UMR 5026, 87 Avenue du Dr. Albert Schweitzer, 33608 F Pessac Cedex, France

[b] Université de Bordeaux, Institut des Sciences Moléculaires, UMR 5255 CNRS, 351 Cours de la Libération, 33405, Talence Cedex, France

[c] Solvay, Research and Innovation Center Paris, F-93308, Aubervilliers, France

KEYWORDS: sodium niobates; perovskites; acentric structure; structural distortions; competing bonds; hydrothermal synthesis; second harmonic generation; reducibility.

ABSTRACT: The two room-temperature $NaNbO_3$ polymorphs crystallizing with orthorhombic symmetry have been successfully isolated at using a new preparative method. The pure polar phase, annealed at 600 °C under air after hydrothermal treatment at 200 °C, adopts the $P2_1ma$ space group, whereas the well-known and thermodynamically stable form with the Pbma structure is obtained at higher temperatures under air (T = 950 °C). Thanks to the combination of powder-XRD Rietveld analysis, ^{23}Na solid-state NMR spectroscopy and second harmonic generation studies, structural features of both these polymorphs reveal clear structural differences. The stability of each atom site is investigated by mean of bond distances, Madelung potentials and DFT calculations. The key role of Na atomic positions is highlighted, especially how they influence the $[NbO_6]$ octahedron distortion. In the polar $P2_1ma$-phase, the higher distortion both along the apical axis and the equatorial plane is consecutive to the relaxation of the overall network with the stabilization of Na atoms in two sites sharing the same symmetry. Focusing on oxygen mobility, both polymorphs show distinct reactivities toward reductive heat treatments: as characterized by thermogravimetric analysis and ESR measurements, the Pbma framework is relatively insensitive, while the $P2_1ma$ one yields a non-stoichiometric oxide with a Nb^{4+} content of 18 % corresponding to $NaNbO_{2.91}$ chemical composition. The fine control in phasic purity together with advances on the structural features of room-temperature phases should benefit both non-linear optical applications and photocatalytic performances of sodium niobates.

INTRODUCTION

The lead-free alternatives to the piezoelectric material $PbZr_{1-x}Ti_xO_3$ (PZT) have been widely investigated these last 15 years;[1–4] among them, $K_xNa_{1-x}NbO_3$ (KNN) is the most promising solid solution, whereas $Li_{1-x}Na_{1-x}NbO_3$ (LNN) phases also display interesting ferroelectric properties at low Li contents ($x < 0.15$).[5,6] The composition and temperature dependences of KNN and LNN oxides have been largely explored, with complex structural features associated to various tilting modes of $[NbO_6]$ octahedra in these derived perovskite networks.[6–8] The common elements Na and Nb in these series combined to the occurrence of various polymorphs at room temperature naturally leads to focus specifically on the end member $NaNbO_3$.[9–13] This composition has attracted interest more recently as a photocatalyst for several reactions, namely hydrogen evolution,[14–17] CO_2 reduction[14,15,18,19] and degradation of various organic molecules.[20–23] In the final catalyst consisting of the niobate alone or combined to other species, the structural variety of $NaNbO_3$ has again been demonstrated to have a strong impact on the catalyst efficiency, especially between the centrosymmetric orthorhombic structure and the cubic one.[14,15] Interestingly, all the catalyzed reactions involve oxygen-based small species as intermediates, underlying the role of oxygen deficiency and mobility in sodium niobates.[23] However, to our knowledge, some polymorphs of $NaNbO_3$ are still to be investigated, e.g. the acentric room-temperature polymorph crystallizing in an orthorhombic space group.

Several authors mention the occurrence of at least seven allotropic forms of $NaNbO_3$ as a function of temperature from 930 to 15 K, corresponding to cubic, tetragonal, orthorhombic and rhombohedral space groups related to the perovskite network.[24–27] The high- and room-temperature phase transitions are mainly consisting in the tilting of the $[NbO_6]$ octahedra, whereas the low-temperature transitions are associated

to the off-centered displacements of niobium atoms as well as the distortion of the [NbO_6] octahedra. It must be pointed out that similar Madelung energies or free energies of all these varieties account for competing structural instabilities, giving rise to all these allotropic forms.[28,29] However, as far as the accurate structure determination is concerned, the main difficulties arise from the slight differences between diffraction patterns especially for the phases which stabilize around room temperature.[26,30] In order to find the best model for structural analysis of $NaNbO_3$ at room temperature, complementary experimental techniques are necessary. The combination of structural refinements from X-Ray powder Diffraction (XRD) and ^{23}Na solid-state Nuclear Magnetic Resonance (NMR) measurements to probe the local environments of sodium ions allows solving these ambiguities. In addition, the specific technique of optical Second Harmonic Generation (SHG) is useful in the case of compounds that do not possess inversion symmetry. Moreover, Madelung potentials and Density Functional Theory (DFT) calculations allow extracting the stability and bonding of each atomic site. All these slight differences of $NaNbO_3$ allotropic forms must be critically described in regard of their reactivity and their optical band gap, which give valuable information about the chemical bonding and the consequences of the K^+ or Li^+ substitution for Na^+ in the case of KNN and LNN piezoelectric and ferroelectric phases, but also on surface activity towards several catalyzed reactions.

Depending on the synthesis route, solid-state approach and sol-gel techniques for instance, two varieties are observed at room temperature.[30] Both structures are distorted perovskites network. Accordingly, the Goldschmidt tolerance factor, describing the deviation to the ideal cubic structure using a geometrical argument, is 0.97 for $NaNbO_3$, taking into account ionic radii of from Shannon et al. with $r(Na^+[XII]) = 1.39$ Å, $r(Nb^{5+}[VI]) = 0.64$ Å and $r(O^{2-}[VI]) = 1.40$ Å.[31,32] The first form crystallizing in the orthorhombic system and Pbma space group is the most cited in the literature with $a = a_p\sqrt{2}$, $b = 4a_p$, $c = a_p\sqrt{2}$, where $a_p \approx 3.9$ Å represents the lattice parameter of the idealized cubic perovskite.[33] Three independent [NbO_6] octahedra tilts occur in this supercell that also contains two crystallographic distinct Na sites. By applying an electrical field, an acentric ferroelectric phase is detected.[34] This polar phase crystallizes also in the orthorhombic symmetry in the $P2_1ma$ space group, but the smaller unit cell with a twice smaller b parameter ($a \approx a_p\sqrt{2}$, $b \approx 2a_p$, $c \approx a_p\sqrt{2}$) is associated with less tilting modes for [NbO_6] octahedra. In addition, several authors mention that the number of phase transitions in $NaNbO_3$ vary as a function of particle size and that $NaNbO_3$ with submicrometer particle sizes favors the polar $P2_1ma$ space group at room temperature.[35,36] By sol-gel technique, starting with Na and Nb alkoxides followed by annealing under air at T = 950 °C, a probably monoclinic phase strongly related to the orthorhombic space group $P2_1ma$ can be stabilized.[30,37] Indeed, high resolution X-ray and neutron powder diffraction patterns reveal slight deviations from $P2_1ma$ space group. However, ^{23}Na solid-state NMR and second harmonic generation measurements confirm the occurrence of a polar phase. Furthermore, a mixture of the two orthorhombic varieties, Pbma and $P2_1ma$, is systematically obtained at room temperature when starting with a classical solid-state route after several grinding and annealing under air up to T = 950°C.[30] Then, a question remains unanswered: which synthesis route would stabilize separately the two orthorhombic forms at room temperature, in order to perfectly characterize their structural features, their reactivity and their optical properties?

In this paper, we implement another synthesis route to stabilize the two orthorhombic varieties as pure phases at room temperature. A comparative study then highlights their relative stability as well as their distinct reactivity and optical properties, which are discussed consequently to their structural differences. On the basis of powder XRD Rietveld analysis and ^{23}Na solid-state NMR investigation, the local distortion of [NbO_6] octahedra, their tilting as well as the Na^+ local environments are described. The chemical bonding and the stability of all atomic sites are evaluated using various models: (i) Madelung potentials are calculated based on an ionic model and (ii) partial and total densities of states are obtained from DFT. Diffuse reflectance spectra of both oxides allows to compare their optical band gap. As the dominant SHG interaction mechanism exists only in materials that lack inversion symmetry, the SHG intensity versus the incident power is measured for both oxides in the Pbma (centrosymmetric) and $P2_1ma$ (acentric) space groups. Finally, Thermogravimetric Analysis (TGA) under $Ar:H_2$ (95:5 %vol.) and Electron Spin Resonance (ESR) allow quantifying the Nb^{5+} reduction into Nb^{4+} related to the stability of the Nb site in both polymorphs.

RESULTS AND DISCUSSION

Phase selectivity among room-temperature polymorphs. In a first step, a Rietveld refinement was carried out on powder obtained after hydrothermal route in autoclave at 200 °C before annealing under air. Considering separately the two structural hypotheses, Pbma and $P2_1ma$ (Supporting Information, Figure S1), the fit remains unsatisfactory. The differences appear clearly on XRD patterns by analyzing the key low intensity peaks between $35° < 2\theta < 45°$. Finally, a phase mixture with 2/3 of Pbma and 1/3 of $P2_1ma$ structural hypotheses leads to the best fit with remarkable accordance in the $35° < 2\theta < 45°$ region. The sample consisting of a mixture of two phases was then annealed under air at either T = 600 °C during 6 h or at T = 950 °C during 24 h, yielding a white powder in both cases. Rietveld refinements of XRD data revealed an excellent fit to the $P2_1ma$ and Pbma space groups, respectively, as observed on Figure 1. The key inset in the $35° < 2\theta < 45°$ region clearly shows the good agreement of the refinements in both cases considered separately, but also the difference between the two space groups. Indeed, both structures are very similar and thus, their XRD pattern are similar as well.

The main difference consists in the cell parameter b being twice as large in the Pbma case. Consequently, inter-reticular planes (hkl) with k-odd Miller indices in Pbma space group have no equivalent in the $P2_1ma$ space group, and thus no signal is detected at the 2θ angles corresponding to their Bragg distance d_{hkl}. Accordingly, Table 1 displays good reliability factors of the Rietveld refinements with similar cell parameters and atomic positions in both cases, after the doubling of the b cell parameter has been taken into account. The higher crystallinity of the Pbma phase synthesized at T = 950°C for 1 day (average coherent domain size around 170 nm) is qualitatively observed on the XRD patterns with narrower peaks compared to the oxide crystallizing in the $P2_1ma$ space group (average coherent domain size around 120 nm) and obtained at lower temperature (T = 600 °C) during a shorter time (6 h). As mentioned in the literature, $NaNbO_3$ undergoes a particle-size-induced phase transition from Pbma to $P2_1ma$ space group.[35,36] Limited temperature and time applied during the annealing are clearly key aspects to control crystal size expansion and thus monitoring the phase purity. More importantly, coupling a hydrothermal route and an annealing treatment under air at various temperatures happens to be a very simple method to access both pure $NaNbO_3$ polymorphs at room temperature, and especially in the $P2_1ma$ space group.

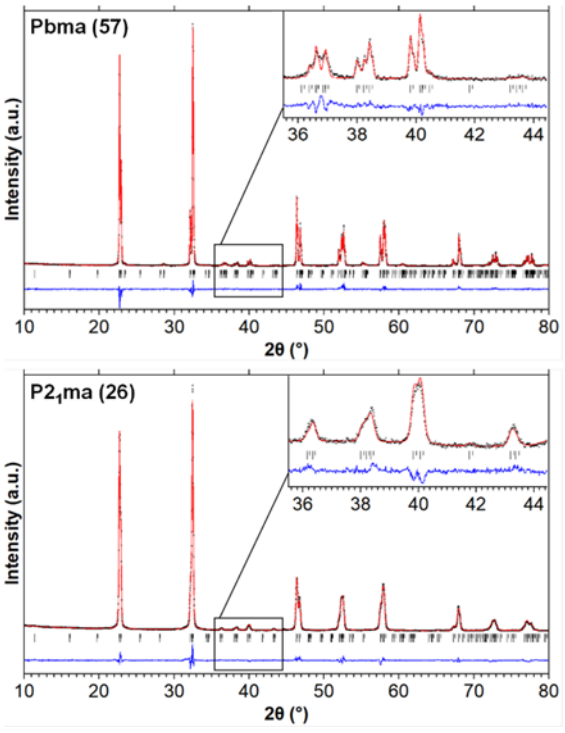

Figure 1. Powder XRD Rietveld refinements of $NaNbO_3$ structures crystallizing in the Pbma and $P2_1ma$ space groups, obtained after hydrothermal synthesis at T = 200°C during 24 h followed by heat treatment under air at 600 °C during 6 h and 950 °C during 24 h, respectively. Insets: zoom of the powder XRD patterns in the region $35.5 \leq 2\theta \leq 44.5$ °.

Table 1. Refined unit-cell parameters and atomic positions of $NaNbO_3$ structures in the Pbma and $P2_1ma$ space groups.

		Pbma air, 950 °C	$P2_1ma$ air, 600 °C
a (Å)		5.5693(3)	5.5601(7)
b (Å)		15.5177(1)	7.7705(10)/15.541[a]
c (Å)		5.5046(3)	5.5142(7)
V (Å³)		475.72(7)	238.24(9) / 476.48[a]
ε (nm)		174(3)	117(3)
Rp (%)		4.15	3.90
wRp (%)		5.33	5.28
Rall (%)		4.27	5.10
Nb	x	0.26979(16)	0.2619(3)
	y	0.1249(2)	0.2510(5)
	z	0.2423(3)	0.2496(9)
Na1	x	0.75	0.272(4)
	y	0	0
	z	0.2606(14)	0.746(4)
Na2	x	0.7853(10)	0.291(2)
	y	0.25	0.5
	z	0.2611(15)	0.750(4)
O1	x	0.25	0.229(4)
	y	0	0
	z	0.302(2)	0.290(3)
O2	x	0.2494(18)	0.193(3)
	y	0.25	0.5
	z	0.176(2)	0.151(3)
O3	x	0.0343(15)	0.034(3)
	y	0.1460(5)	0.275(2)
	z	0.5327(11)	0.551(3)
O4	x	0.4602(12)	-0.032(3)
	y	0.1134(6)	0.229(2)
	z	-0.0417(11)	0.016(3)
β_{iso}(Nb) (Å²)		0.5	0.5
β_{iso}(Na) (Å²)		1	1
β_{iso}(O) (Å²)		1	1

There is a clear structural relationship between these frameworks, taking into account the doubling of the b cell parameter for the Pbma hypothesis. The atomic networks are further compared from the point of view of distortions by means of Nb-O bond lengths (Figure 2). Along the b direction, the O2-Nb-O1 bonding is more distorted in the $P2_1ma$ space group, with a long Nb-O2 distance (2.05 Å) compared to Nb-O1 in the same structure, but also compared to both Nb-O1 and Nb-O2 in Pbma space group (1.97 and 1.98 Å). In both allotropes, $[NbO_6]$ exhibits a second distortion perpendicular to the b axis which involves infinite O_4-Nb-O_3-Nb-O_4 bond sequences in the equatorial plane with alternating long (ca. 2.1 Å) and short (ca. 1.9 Å) bonds (red distances in Figure 2a). However, this distortion is more pronounced for the $P2_1ma$ polymorph, as the absolute deviations from average distance value are systematically higher than for Pbma (red values in Figure 2b). The second order Jahn-Teller (JT) effect of Nb^{5+} ions arises from mixing vacant 4d-character conduction bands and filled 2p-character valence bands. It occurs when the d levels are sufficiently lowered as the cation becomes smaller and more highly charged. It is induced in structures with relatively low bandgap energy such as sodium niobiates with perovskite frameworks. This aspect is further

discussed in the forthcoming paragraph related to the optical band gap and associated figures. Then a spontaneous second-order JT distortion can be observed in the $P2_1ma$ and Pbma polymorphs. It is important to analyze the reason for the $[NbO_6]$ octahedron to be more distorted in the $P2_1ma$ network, although it is prepared at lower temperatures. Looking closely at Na sites, both phases display two structurally distinct coordination sites Na1 and Na2. Average bond distances <Na1-O> and <Na2-O> are almost identical in the $P2_1ma$ structure but rather different in the Pbma network (Table S1). The largest average bond distance is identified for <Na1-O> in the Pbma space group corresponding to the Na1 coordination site with a rotation axe, a symmetry operator that is exclusive to this Na site.

a

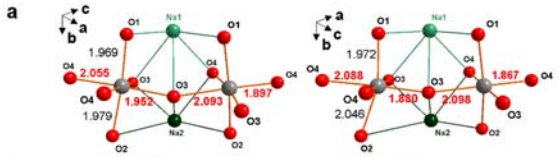

b

	Pbma		$P2_1ma$	
Oi	d(Nb-Oi) (Å)	Δ to avg (%)	d(Nb-Oi) (Å)	Δ to avg (%)
O1	1.969(4)	-1.1	1.972(5)	-1.0
O2	1.979(4)	-0.6	2.046(7)	+2.7
O3	1.952(8)	-2.0	1.880(2)	-5.6
O3	2.093(7)	+5.1	2.098(2)	+5.4
O4	1.897(7)	-4.7	1.867(2)	-6.2
O4	2.055(7)	+3.2	2.088(2)	+4.8

Figure 2. $[NbO_6]$ octahedra distortion of $NaNbO_3$ structures for Pbma and $P2_1ma$ space groups. a) Each structure displays two adjacent octahedra with Nb atoms at the center (grey) and Nb-Oi distances in angströms for i = 1, 2 (black) and i = 3, 4 (red); b) table of Nb-Oi distances and deviation to average for each structure, red values highlight higher absolute deviations for the phase in $P2_1ma$ space group.

The local environments of sodium atoms were further investigated using ^{23}Na solid-state NMR. Sodium nuclei, with a nuclear spin quantum number $I = 3/2$, carry an electric quadrupole moment $Q = 10.4$ fm^2. As a consequence, they are highly sensitive to Electric Field Gradient (EFG) arising from a non-spherical distribution of the electric charges around the nuclei. Then, ^{23}Na NMR spectra, including central and satellite transition lines, may be of complex shape. This is reflected by the strength of the quadrupolar interaction and the anisotropy of the EFG. Nonetheless, spectra can be simulated considering the effects of first and/or second order quadrupolar interactions. Such a simulation depends of three main parameters: δ_{iso} the isotropic chemical shift, C_Q the quadrupolar coupling constant ($C_Q = 0$ for spherically symmetric EFG) and η_Q the asymmetry parameter of the EFG ($0 \leq \eta_Q \leq 1$; $\eta_Q = 0$ for axially symmetric EFG). ^{23}Na MAS NMR spectra of both $NaNbO_3$ polymorphs are presented on Figure 3 (black lines). Each spectrum can be described as the sum of two components (green subspectra) characterized by different sets of δ_{iso}, C_Q and η_Q parameters (Table 2) and associated with two distinct Na site environments. The structural features clearly show that Na2 sites in Pbma and $P2_1ma$ space groups (4d Wyckoff position in Pbma and 2b Wyckoff position in $P2_1ma$) share the same mirror symmetry and the absence of rotation axis of symmetry, while Na1 coordination sites are characterized by a different rotational symmetry with a C_2 axis in Pbma space group (4c Wyckoff position in Pbma and 2a Wyckoff position in $P2_1ma$). Thus, the NMR subspectra with $C_Q = 1$ MHz and $\eta_Q = 0.8$ (deep green components in Figure 3) can be associated with Na2 sites while the other subspectra (light green) are unambiguously attributed to Na1 sites where the sodium nuclei are influenced by more or less asymmetric electric field gradients. The asymmetry parameter of the EFG tensor η_Q is a measure of deviation from cylindrical symmetry. Accordingly, it is close to 0 for Na1 sites in Pbma polymorph and close to 1 for Na1 sites in $P2_1ma$ (Table 2). Moreover, the values reported in Table 2 are in good agreement with theoretical and experimental data from the literature predicting the same site assignement.[30] Comparing experimental 1D ^{23}Na MAS-NMR spectra, both phases are distinguished in the chemical shift region $-30 < \delta < -20$ ppm, where Na1 component is exclusively detected.

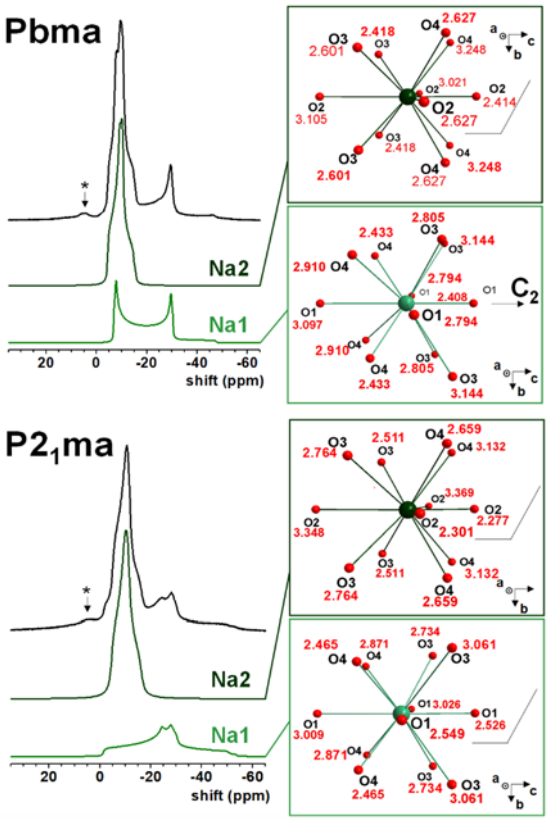

Figure 3. ^{23}Na solid-state NMR of $NaNbO_3$ structures in the Pbma and $P2_1ma$ space groups and Na local environments calculated from powder XRD Rietveld refinements. ^{23}Na MAS (10 kHz) NMR experimental spectra (black) and simulated signals (deep and light green) associated with the two Na sites. Structures: sodium (deep and light green) surrounded by oxygen with Na-O

distances (red, Å). Planar or rotational symmetry operators are represented for each Na site. *unidentified signal.

Table 2. ^{23}Na NMR parameters of Na1 and Na2 sites in Pbma and P2$_1$ma space groups: the isotropic chemical shift δ_{iso}, the quadrupolar coupling constant C_Q and the asymmetry parameter of the electrical field gradient η_Q.

	Pbma		P2$_1$ma	
	Na1	Na2	Na1	Na2
δ (ppm)	-0.9(4)	-4.6(4)	-1.5(4)	-5.3(4)
C_Q (MHz)	2.2(1)	1.0(1)	2.1(1)	1.0(1)
η_Q	0.0(1)	0.8(1)	0.8(1)	0.8(1)

The two Na sites exhibit different symmetries in the Pbma space group, whereas they share the same mirror symmetry in the case of P2$_1$ma. The absence of rotational symmetry for the two Na coordination sites in the polar phase, P2$_1$ma, creates less constraints in the network and, consequently, the [NbO$_6$] octahedron distortion is higher. On the basis of competitive bonds along Na-O-Nb or inductive effects around O^{2-} ligands in the perovskite network, the stabilization of a larger (Na1) and a smaller (Na2) coordination sites with two various symmetries in Pbma structure contributes to decrease the [NbO$_6$] second order Jahn-Teller distortion. The driving force of second Jahn-Teller distortion of the [NbO$_6$] octahedron is then the degree of liberty and site symmetry of Na local environments. The symmetry of NaNbO$_3$ weakens from Pbma to P2$_1$ma space group as well as the crystallinity (annealing under lower temperature and shorter time), whereas the [NbO$_6$] octahedron distortion in the metastable P2$_1$ma phase increases thanks to the flexibility of the network and especially the Na coordination sites. Importantly, ^{23}Na NMR experiments confirm the XRD results that evidenced the phase selectivity of the chosen synthesis routes.

Phase selectivity can also be assessed by measurement of optical non-linear properties of the structure in the P2$_1$ma space group. Optical Second Harmonic Generation (SHG) is a process that combines two photons of an incident wave at frequency ω, into a single photon of frequency 2ω. The dominant electric-dipole SHG interaction involves three photons, two input photons of frequency ω, both taken from the same laser source, and one output photon at frequency 2ω, which can occur only in materials that do not possess inversion symmetry. SHG measurements of the intensities backscattered can be recorded as a function of the incident power to determine the quadratic coefficient of the non-linear optical response and perform relative quantitative measurements of the susceptibility of a material. Such non-linear optical quantitative 3D µ-imaging measurements in a spin-crossover micro-crystallite have been successfully applied in the past.[47] A generalization of this previous semi-quantitative approach can also be applied to a statistic assembly of micro-crystallites with an average granulometry:

$$I_{2\omega} \propto N. < \chi_{eff}^{(2)} >^2 I_{\omega}^2, \qquad (1)$$

where N is the number density of micro-crystallites. It allows to quantify the slope of the quadratic dependence of the SHG intensity with the incident power, slope which is proportional to the square of the average effective non-linear optical susceptibility $< \chi_{eff}^{(2)} >$. Note that this experimental procedure is quite different but complementary to the well-known method developed by Kurtz and Perry in the late 1960's.[48] SHG quantitative measurements were performed on both oxides crystallizing with the Pbma and P2$_1$ma space groups and are reported on Figure 4. The intensity of back-scattered photons at 2ω is plotted as a function of the incident source power at ω and fit nicely the quadratic function given by Equation 1. The phase annealed at T = 600 °C, which adopts the acentric orthorhombic P2$_1$ma network, exhibits a very intense SHG active signal, with a slope 100 times higher than the other oxide annealed at higher temperatures. The signal detected in this case cannot be attributed to the centrosymmetric structure in Pbma space group. It could be due to P2$_1$ma contamination, which then, following Equation 1, would be ca. 1 %vol., since the density of the two forms are very similar. Another possibility is the local surface polarization of small molecules, such as water, which would provide acentric species to generate an induced second harmonic signal. The surface charge density and the associated potential are important characteristics of interfaces. This interfacial contribution is a Kerr contribution called Electric Field Induced Second Harmonic (EFISH) which involves the third-order susceptibility $\chi^{(3)}$ of the material (which is strong for such perovskites materials) and the interfacial potential. Despite the fact that the origin of this residual signal remains unclear, SHG is in agreement with powder XRD Rietveld and ^{23}Na NMR data, confirming unambiguously the stabilization of two pure polymorphs of NaNbO$_3$ at room temperature. They share a lot of structural similarities, however some differences must be pointed out, such as the distortion of Nb site and symmetries of Na sites, in addition to the well-known absence of inversion center in the case of a P2$_1$ma space group. In the following section, the stability of all atomic sites in the polymorphs are compared using energy calculations, and the occurrence of the metastable acentric phase is discussed.

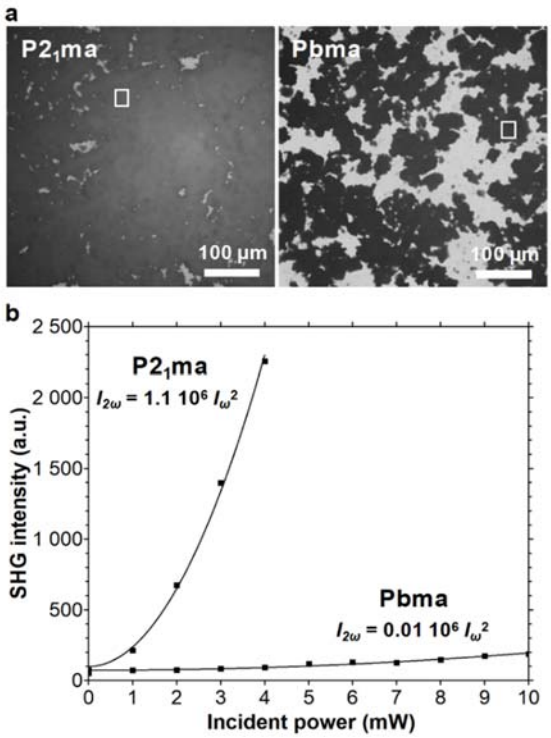

Figure 4. a) Bright field pictures of the powders with selected areas (white rectangles) for SHG analysis. b) SHG of $NaNbO_3$ structures in the Pbma (centrosymmetric) and $P2_1ma$ (acentric) space groups.

Energy considerations. In order to investigate site energies and chemical bonding in $P2_1ma$ and Pbma frameworks, two approaches were considered. The first one, based on a simple ionic model,[40] allows calculating the Madelung potential of each crystallographic site, whereas the second one consists in determining the partial and total density of states (DOS), giving access to the center of gravity of the partial DOS of each non-equivalent atom. As reported in Table 3 for niobium and oxygen, the relative stability of atoms or atomic sites follows the same trend in both approaches. Table 4 shows that whatever the space group, the Na1 site is the most unstable from the point of view of Madelung potential, and the differences in Madelung potentials and average energy between Na1 and Na2 crystallographic site are larger in the Pbma structure. The lowest absolute potential and energy are obtained in this space group, for the Na1 site involving a rotational symmetry. Furthermore, the Madelung potential and average energy of O1 species in the vicinity of this Na1 site are the highest among the four oxygen positions. Lastly in the Pbma space group, the same effect is observed with the stabilization of Na2 site and the destabilization of O2 atomic position in the vicinity of Na2. Concerning the $P2_1ma$ space group, the Madelung potentials and average energies of Na1 and Na2 sites are closer. The stability of O1 and O2 apical sites are also closer but in average lower than in Pbma space group. Besides, the higher the absolute values of potentials and energies of Na1 (Na2) site, the lower the values of O1 (O2) environment. In both structures, the two Na1 and Na2 atomic positions thus strongly influence O1 and O2, i.e. the apical oxygen atoms in the $[NbO_6]$ octahedron.

Table 3. Madelung potentials (V_M) and average valence energies (<*E*>) with respect to the Fermi level, for Nb and O atomic sites in $NaNbO_3$, in the Pbma and $P2_1ma$ space groups. <*E*> values were calculated from DFT. The experimental crystal structures were used as input for all calculations.

	Pbma		$P2_1ma$	
site/atom	V_M (V)	<E> (eV)	V_M (V)	<E> (eV)
Nb	-52.0	-3.676	-52.1	-3.779
O1	+27.1	-2.841	+25.7	-2.842
O2	+23.9	-2.225	+23.6	-2.108
O3	+24.3	-2.257	+26.2	-2.850
O4	+25.7	-2.673	+24.6	-2.503

Table 4. Madelung potentials (V_M)) and average energies (<*E*>) of Na 3s-character bands, in the Pbma and $P2_1ma$ space groups. <*E* > values were calculated from DFT.

	Pbma		$P2_1ma$	
site/atom	V_M (V)	<E> (eV)	V_M (V)	<E> (eV)
Na1	-11.6	+11.80	-12.8	+11.93
Na2	-15.0	+12.49	-13.8	+12.13

Regarding oxygen sites in the equatorial planes, the O3 is more stable in the $P2_1ma$ network, while O4 is more stabilized in the Pbma space group. However, by considering average Madelung potentials and energies between O3 and O4, it appears that the oxygen atoms in the equatorial planes are more stable in the $P2_1ma$ framework. Furthermore, the average potentials and energies between O1 and O2 sites are higher in the Pbma than in the $P2_1ma$ networks. O2 and O3 are the most unstable in the Pbma structure, whereas only the O2 atomic position is clearly the unstable anionic species in the $P2_1ma$ network. Finally, a stabilization of the apical oxygen atoms in the phase of Pbma space group (higher potentials and energies of O1 and O2) is accompanied by a destabilization of equatorial oxygen atoms (lower potentials and energies of O3 and O4). This effect of apical oxygen destabilization in the $P2_1ma$ space group contributes, by competing interactions, to stabilize the O3 and O4 oxygen atoms in the equatorial planes (average values).

The total DOS of $NaNbO_3$ in the Pbma and $P2_1ma$ structures are depicted on Figure 5, as well as partial DOS for non-equivalent sodium and oxygen atoms. The partial DOS for Na atoms (Figure 5a) shows clear differences between $P2_1ma$ and Pbma structures in the low energy region of 3s-character bands, which especially reveals again the clear differentiation of Na1 and Na2 in the Pbma space group. For oxygen sites (Figure 5b), the partial DOS contribution around the Fermi level in the Pbma framework shows the higher instability of O3 compared to the other ones, in agreement with the previous analysis. In the $P2_1ma$ network, the O2 atomic position in the vicinity of Na2 is the most unstable, as mentioned in the previous paragraph. The total DOS in the Pbma and $P2_1ma$ frameworks (Figure 5c) displays very close band gaps around 3.5 eV, with a more pronounced band edge in

the case of Pbma. A slightly higher band gap is expected for the $P2_1ma$ structure associated to a slightly lower crystal field splitting of Nb^{5+}(4d). Accordingly, diffuse reflectance spectra of the two polymorphs, represented on Figure 6, confirm band gaps both at ca. 3.4 eV, though slightly higher in the $P2_1ma$ network.

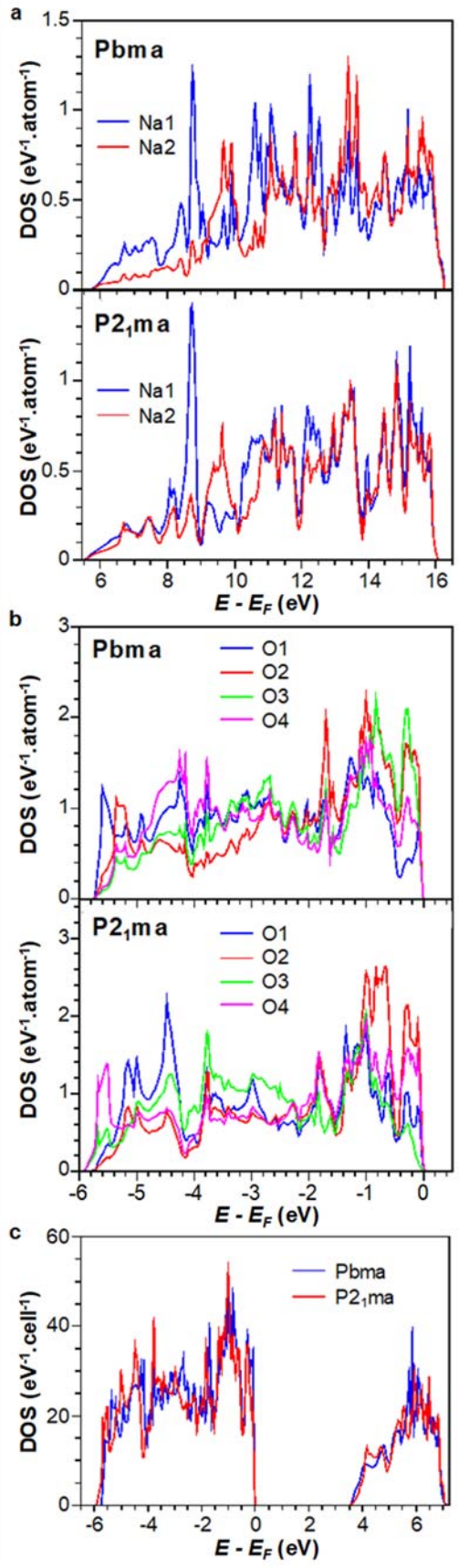

Figure 5. Partial and total density of states of $NaNbO_3$ in the Pbma and $P2_1ma$ space groups. a) Na1 and Na2, b) O1, O2, O3 and O4, and c) total density of states.

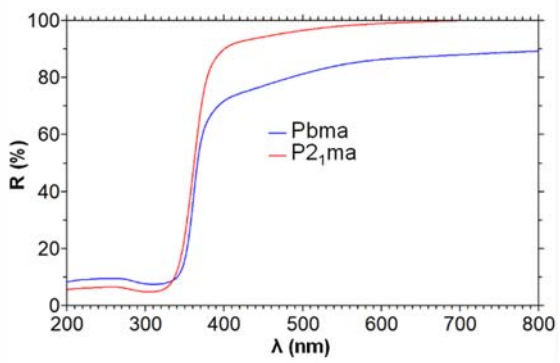

Figure 6. Diffuse reflectance of $NaNbO_3$ after hydrothermal synthesis followed by annealing 6 h at 600 °C ($P2_1ma$) and 24 h at 950 °C (Pbma).

All in all, taking into account the structural study and relative stability considerations, the relaxation of equatorial Nb-O bond distances in the $P2_1ma$ framework is associated to similar Na1 and Na2 sites (stability and symmetry), leading to the destabilization of O1 and O2 apical oxygen atoms, especially O2 in the vicinity of Na2. These effects, which are not found in the Pbma structure, are key parameters to understand the stabilization of the lower symmetry structure in the $P2_1ma$ space group. Calculations confirm the strong influence of Na chemical bonding which contribute to perturb the Nb^{5+} second-order Jahn-Teller distortion in $NaNbO_3$. From these results, it is pertinent to question the mobility of oxygen in two overall closely related perovskite-derived anion networks, with one of them exhibiting adjacent oxygen sites that are more similar, although more destabilized. Niobium being prone to stabilize the +IV oxidation state ($4d^1$), the reducibility of sodium niobates vs. their crystal structures is investigated in the following part.

Reducibility of sodium niobates. Reduction processes under a gas mixture of argon and dihydrogen ($Ar:H_2$ = 95:5 %vol.) were followed by thermogravimetric analysis during a heat treatment consisting of a 3 °C·min^{-1} ramp, to a temperature of 1000 °C that was maintained 1 h. The curves on Figure 7 show striking differences in term of weight loss upon such treatment: no significant weight loss is detected in $NaNbO_3$-Pbma during the whole experiment, whereas $NaNbO_3$-$P2_1ma$ experiences a continuous weight loss up to 500 °C; then, the weight stabilizes before strongly decreasing from 800 °C. ESR spectra of the two resulting samples are reported on Figure 8. The reduction treatment of $NaNbO_3$-Pbma at high temperature results in two superimposed signals associated with a low content of paramagnetic centers. The signal complexity is the consequence of anisotropic *g*-values and spectral overlap of hyperfine *(h.f.)* and superhyperfine *(s.h.f.)* structures arising from *h.f.* interaction with ^{93}Nb nuclear spin (I = 9/2) and *s.h.f.* additional interaction with ^{23}Na nuclear spins (I = 3/2). Nonetheless, the average value of *g*-factor (≤ 2), the values of hyperfine coupling constants (≤ 10 mT), the observation of ^{23}Na superhyperfine structure and the linewidth (≤ 1 mT) suggest that they are due to paramagnetic centers such as surface defects involving Nb^{4+}, unpaired electrons or holes located on the oxygen atoms and/or oxygen vacancies.[49,50] Based on ESR data, the concentration in paramagnetic centers was roughly estimated at 100±20 ppm. The expected weight loss associated to oxygen removal during such a reduction is of the order of 0.0001 %, which is not significant with respect to the sensitivity of the TGA apparatus. Regarding $NaNbO_3$-$P2_1ma$ treated in the same reductive conditions, a broader signal in the same magnetic field region is detected by ESR. It is attributed to a Nb^{4+} concentration several orders of magnitude higher in this polymorph, high enough to generate strong dipolar interactions and magnetic coupling at the origin of the signal broadening. Accordingly, the color of the $Ar:H_2$ treated sample vary from light blue-grey for $NaNbO_3$ originally in the Pbma space group to dark grey for $P2_1ma$. For the latter, no quantification was possible from ESR. Based on the weight loss from 800 °C (Figure 7), the deduced composition after reduction is $NaNbO_{2.91}$, i.e. 18% of Nb^{4+}. This non-stoichiometric oxide with Nb mixed valence crystallizes with the Pbma space group (Figure S2). Such a phase transition is not surprising, given the temperature achieved during the reductive treatment. The weight loss at lower temperatures during the heat treatment of $NaNbO_3$-$P2_1ma$ is attributed to adsorbed moieties at the surface, such as water and hydroxyl groups.[51] No weight loss is observed starting from Pbma-$NaNbO_3$, even below 500 °C. It could be due to smaller specific surface area for this sample, which corresponds to larger average crystallite size (170 nm instead of 120 nm for $P2_1ma$) and higher annealing temperature (950 °C instead of 600 °C). Indeed, a more pronounced aggregation of larger crystals accounts for significantly less surface area where adsorption occurs. This could then explain the difference in weight loss between both samples, below 500 °C.

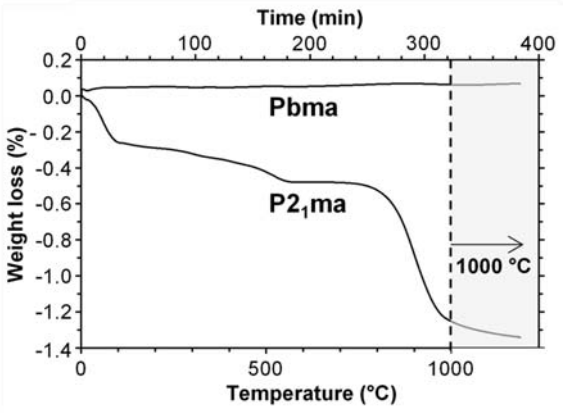

Figure 7. TGA of $NaNbO_3$ structures in the Pbma and $P2_1ma$ space groups under a $Ar:H_2$ mix (95:5).

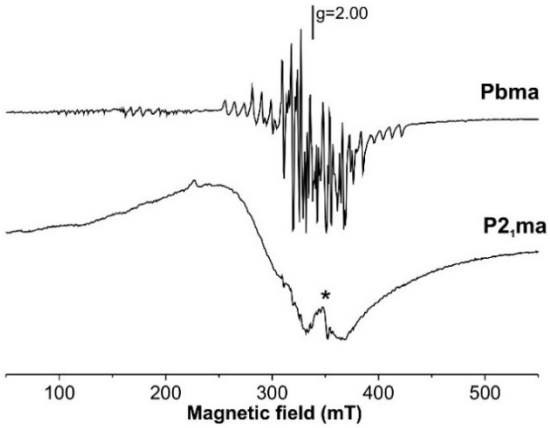

Figure 8. Low-temperature (4 K) X-band ESR spectra of reduced sodium niobates from the Pbma and $P2_1ma$ structures after exposure to a Ar:H_2 mix (95:5 %vol.) at 1000 °C during 1 h. *unidentified paramagnetic signal.

This last investigation demonstrates the higher reducibility of $NaNbO_3$-$P2_1ma$. It is probably related to the distortion of NbO_6 octahedra in this framework, where Na sites acts indirectly by competing bonds on Nb-O chemical bonding. The Nb^{4+} rate stabilized in the $P2_1ma$ network remains unusually high in this perovskite-related network and might be even increased if the structure in $P2_1ma$ space group is maintained after the treatment, for instance by optimizing the conditions of the reductive treatment. The reducibility of Nb in $NaNbO_3$ is also necessarily connected to oxygen mobility. O3 and O4 sites are always closer to the Nb site than O1 and O2. On the basis of energy considerations and previous calculations, it is hypothesized that O2 sites are the most prone to participate to oxygen diffusion in $P2_1ma$ network The reduction treatment of Pbma phase in the same conditions show this composition is stable without the formation of oxygen vacancies (only 100 ppm of Nb^{4+} determined by ESR measurements leading to consider the quasi-absence of oxygen vacancies). Then, the oxygen and sodium sites stabilities, strongly connected to the creation of oxygen vacancies, affect the Madelung energy of P21ma polymorph which is lower than of Pbma form. In $NaNbO_{2.91}$, it was not possible to localize O-vacancies based on XRD data (Figure S2). Intense XRD light (synchrotron) and neutron sources will be required to further investigate structural features of mixed valence sodium niobates, as well as possible occurrence of phase transitions vs. temperature. Moreover, the control of mixed valence ratios and oxygen mobility in room-temperature polymorphs of $NaNbO_3$ rises questions concerning the photocatalytic properties that recently attracted interest for $NaNbO_3$, especially in hydrogen evolution, CO_2 reduction and degradation of organic molecules.[14–23] Future works focusing on phasic purity should enable to better understand catalytic properties of sodium niobates and improve their performance.

CONCLUSION

In summary, a new selective synthesis route has been presented towards the two polymorphs of $NaNbO_3$ at room temperature. A thorough and detailed investigation of both phases by powder XRD, ^{23}Na solid-state NMR and SHG complementary analyses revealed without ambiguities the formation of a pure polar phase which crystallizes with the $P2_1ma$ space group at relatively low temperature (600 °C). This oxide transforms irreversibly at higher temperature (below 950 °C) into the thermodynamically stabilized compound which adopts the centrosymmetric Pbma space group. Despite the similarities of XRD patterns of both these forms, the $[NbO_6]$ octahedron distortion and complex octahedral tilt schemes have been described and discussed. Significant structural changes were pointed out. The second order Jahn-Teller distortion of Nb^{5+} ($4d^0$) is exalted in $P2_1ma$ network where the two Na atom sites display the same mirror symmetry. In the Pbma space group, the Na atoms are located in two sites with distinct symmetry. Both Na sites contribute by competing bonds to constrain $[NbO_6]$ octahedron to be less distorted but more rigid in the Pbma framework. On the contrary, for the polar phase, the large difference of the two apical Nb-O bond lengths and the alternation of longer and shorter Nb-O bond distances in the equatorial plane underline the relaxation of the $P2_1ma$ network, though more distorted. This is due to the key role of Na atomic positions which influence indirectly the second order Jahn-Teller distortion of $[NbO_6]$. Madelung potentials and exploration of partial density of states by DFT allowed identifying the site stability and the differences in chemical bonding. Both approaches clearly show the effect of sodium on the oxygen atoms and their consequence on the $[NbO_6]$ tilt and distortion. The optical band gap of both these polymorphs are very similar but the energy is slightly higher for the polar phase, in good agreement with the total density of states around the Fermi level calculated by DFT. The structural features of $NaNbO_3$ polymorphs, and especially the relaxation of the network and the distortion of NbO_6 octahedron, are discussed in the light of drastically distinct reactivities upon reduction treatments. The thermodynamically stabilized form (Pbma space group) of $NaNbO_3$ is not affected by heat treatments under Ar:H_2 (95:5 %vol.) up to 1000 °C, whereas a large content of Nb^{4+} (18 %), detected by TGA and ESR, is stabilized in the centrosymmetric perovskite network with a composition $NaNbO_{2.91}$, starting from $NaNbO_3$-$P2_1ma$. These preparative methods and consecutive characterizations shed new light on several existing fields of research regarding sodium niobates, especially (i) in the stabilization at low temperature of LNN and KNN solid solution, with the influence of polarizing (Li^+) and polarizable (K^+) species on Na sites, leading to ferroelectric and piezoelectric properties and (ii) concerning photocatalytic processes already demonstrated in various reactions of interest.

EXPERIMENTAL SECTION

Synthesis. 0.810 g of Nb_2O_5 (99.9 %, Sigma-Aldrich) was dispersed in 20 mL of NaOH 6 M and heated in an autoclave equipped with 40 mL Teflon vials. The sample was heated at 200 °C during 24 h with heating and cooling ramps of 2 °C·min^{-1}. The white sediment and supernatant were both transferred

in a 200 mL centrifuge tube (Nalgene) and centrifuged 15 min at 7 krpm. The supernatant was removed, the pellet was dispersed in ca. 100 mL of deionized water and the dispersion was centrifuged 15 min at 7 krpm. The separation, dispersion and centrifugation steps were repeated once. Finally, the supernatant was removed and the pellet was dried at 80 °C overnight, yielding a white powder. Annealing treatments were performed under air in tubular ovens. $NaNbO_3$ structures crystallizing with Pbma and $P2_1ma$ space groups were obtained after 24 h at 950 °C and 6 h at 600 °C, respectively, with systematic 2 °C·min^{-1} heating and cooling ramps.

Powder X-ray diffraction was performed on a PANalytical X'pert PRO MPD apparatus equipped with an X'Celerator multichannel detector. $CuK\alpha_1/K\alpha_2$ radiations were generated at 45 kV and 40 mA. Data were acquired on the reflection Bragg-Brentano θ-θ mode, $8\ ^\circ \leq 2\theta \leq 80\ ^\circ$ with 0.017 ° steps and acquisition time of 6 h 37 min. The resolution of XRD diffraction lines with this apparatus is equal to 0.08°. Samples were prepared from soften powder (particle size < 45 µm) flattened with the edge of a razor blade to avoid any preferential orientation. Refinements were performed using the JANA2006 software.[38] Rietveld refinements were performed with fixed β_{iso} value of 0.5 for Nb, 1 for Na and 1 for O.

^{23}Na solid-state nuclear magnetic resonance spectra were acquired at a 7.05 T static magnetic field (Larmor frequency: 79.4 MHz) with a single short pulse (π/8) excitation of 1.5 µs (radio frequency field strength: ca. 166 kHz) and a recycling delay of 30 s. Magic Angle Spinning (MAS) experiments were performed at a spinning frequency of 10 kHz with a 4 mm Bruker probe. The resolution of NMR peaks is 0.06 ppm. Chemical shifts were calibrated according to a molar solution of NaCl (δ = 0.0 ppm). Magnitude and anisotropy of electric field gradient of each contribution were refined from experimental data using dmfit software.[39]

Second harmonic generation. Samples were pressed between two glass slides and analyzed with a home-built scanning SHG microscope. The excitation source is a femtosecond laser emitting at 1030 nm (Mikan, Amplitude system), which delivers 250 fs pulses at a repetition rate of 50 MHz. The laser light is focused into the sample with a microscope objective (10X Nikon Plan Fluor, NA = 0.3) and the resultant SHG at the wavelength 1030/2 nm is collected in the backward direction using a photomultiplier tube. Typical large SHG images of 500 x 500 µm^2 where recorded with a spatial resolution of *ca.* 10 µm and with a total acquisition time less than 2 s. SHG images were acquired by incrementing the average incident power between 1 and 10 mW to achieve a semi-quantitative quadratic power law dependence of the powder samples by averaging the SHG response for some selected areas.

Madelung potentials and hybrid DFT calculations. On the basis of the crystal structure determination, the Madelung potentials of each atomic sites were calculated by the Ewald method.[40] In this pure ionic model, atoms are considered as point (formal) charges located at all relevant crystallographic sites. Density functional theory (DFT) calculations were performed using the projector augmented-wave (PAW) method as implemented in the VASP code.[41–43] PAW datasets were used to describe valence electron-ionic core interactions, with valence Na 2s, 3p, Nb 4p, 4d, 5s and O 2s, 2p electrons treated explicitly. The exchange and correlation energies were treated using the generalized gradient approximation (GGA) according to the Perdew-Burke-Ernzerhof formulation,[44] further corrected by the Heyd-Scuseria-Ernzerhof (HSE06) screened hybrid scheme, where 25 % of GGA exchange is replaced by exact Hartree-Fock (HF) exchange.[45,46] The Brillouin zone was sampled using Γ-centered grids of 6×2×6 and 6×4×6 *k*-points for the Pbma and $P2_1ma$ polymorphs, respectively. Calculations were carried out on the two structural models leading to determine the total and the partial density of states (DOS) for each atom. In order to extract an information on the stability and bonding of each atomic site from partial densities of states, and for comparison with Madelung potentials, the center of gravity of the partial DOS (with respect to the Fermi level) can be calculated for each non-equivalent atom, according to:

$$< E > = \frac{\int n_i(E).E.dE}{\int n_i(E).dE} \qquad (2)$$

where $n_i(E)$ is the partial DOS for the atom i. For Nb and O atoms, the integrals run over the valence (2p-character) bands. For Na atoms, the partial DOS in O 2p-character bands is very small, because the Na-O bonding is mostly ionic. Therefore, it is more relevant to examine the Na partial DOS values and center of gravity in the Na 3s-character (empty) bands.

Diffuse reflectance spectra were recorded on powders in the 200-800 nm range using a Carry-Varian 5000 spectrometer equipped with an integrating sphere. MgO powder was used as a white reference.

Thermogravimetric analyses were carried out on a SETARAM Setsys Evolution apparatus under an Ar:H_2 (95:5 %vol.) flux (50 mL·min^{-1}) with a heating rate of 3 °C·min^{-1} up to 1000 °C. The sample was then maintained at 1000 °C for 1 h. Mass fluctuations of a blank sample (empty Pt nacelle) due to the heat treatment were subtracted from the raw signal.

Electron spin resonance experiments were conducted with a Bruker EMX spectrometer operating at X-Band (9.45 GHz) and equipped with a helium flow cryostat. The presented powder spectra were recorded at low temperature (4 K) and normalized to the sample mass (100 mg). The frequency and amplitude of the magnetic field modulation were set to 100 kHz and 0.5 mT, respectively. The magnetic field scale was calibrated using a DPPH standard sample (g = 2.0036) and the Bruker software suite (WinEPR and WinSimfonia) was used to analyze the observed ESR signals.

ASSOCIATED CONTENT

Supporting Information. The following file are available free of charge (Word document): Figure S1. Rietveld refinements of NaNbO3 powder obtained after

hydrothermal synthesis (no annealing); Table S1. Na-Oi distances in NaNbO3 structures in the Pbma and P21ma space groups; Figure S2. XRD pattern of NaNbO3-x after exposure of P21ma-NaNbO3 to Ar:H2 (95:5 %vol.) at 1000 °C during 1 h, and refinement using profile matching method with Pbma structural hypothesis.
Two .cif files (NaNb_Pbma.cif and NaNb_P21ma.cif) have been uploaded as supporting information.

AUTHOR INFORMATION

Corresponding Author

*(A.D.) alain.demourgues@icmcb.cnrs.fr (The ORCID iD registered to your address alain.demourgues@icmcb.cnrs.fr is https://orcid.org/0000-0002-3828-8498) and (G.G.) gougetguillaume@gmail.com, Present Addresses
†(G.G.) Department of Chemistry, University of Pennsylvania, Philadelphia, Pennsylvania 19104, United States.

Author Contributions

The manuscript was written through contributions of all authors. All authors have given approval to the final version of the manuscript.

ACKNOWLEDGMENT

The authors are thankful to Dany Carlier for the discussions on ^{23}Na NMR.

REFERENCES

(1) Saito, Y.; Takao, H.; Tani, T.; Nonoyama, T.; Takatori, K.; Homma, T.; Nagaya, T.; Nakamu, M. Lead-Free Piezoceramics. *Nature* **2004**, *432*, 84–87.
(2) Cross, E. Lead-Free at Last. *Nature* **2004**, *32* (7), 666–668.
(3) Rödel, J.; Jo, W.; Seifert, K. T. P.; Anton, E. M.; Granzow, T.; Damjanovic, D. Perspective on the Development of Lead-Free Piezoceramics. *J. Am. Ceram. Soc.* **2009**, *92* (6), 1153–1177.
(4) Rödel, J.; Webber, K. G.; Dittmer, R.; Jo, W.; Kimura, M.; Damjanovic, D. Transferring Lead-Free Piezoelectric Ceramics into Application. *J. Eur. Ceram. Soc.* **2015**, *35* (6), 1659–1681.
(5) Ringgaard, E.; Wurlitzer, T. Lead-Free Piezoceramics Based on Alkali Niobates. *J. Eur. Ceram. Soc.* **2005**, *25* (12), 2701–2706.
(6) Peel, M. D.; Ashbrook, S. E.; Lightfoot, P. Unusual Phase Behavior in the Piezoelectric Perovskite System, $Li_xNa_{1-x}NbO_3$. *Inorg. Chem.* **2013**, *52* (15), 8872–8880.
(7) Ahtee, M.; Glazer, A. M. Lattice Parameters and Tilted Octahedra in Sodium-Potassium Niobate Solid Solutions. *Acta Crystallogr. Sect. A* **1976**, *32*, 434.
(8) Handoko, A. D.; Goh, G. K. L. Hydrothermal Synthesis of Sodium Potassium Niobate Solid Solutions at 200 °C. *Green Chem.* **2010**, *12* (4), 680.
(9) Cai, B.; Schwarzkopf, J.; Hollmann, E.; Braun, D.; Schmidbauer, M.; Grellmann, T.; Wördenweber, R. Electronic Characterization of Polar Nanoregions in Relaxor-Type Ferroelectric $NaNbO_3$ Films. *Phys. Rev. B* **2016**, *93* (22), 1–8.
(10) Gu, L.; Zhou, D.; Cheng Cao, J. Piezoelectric Active Humidity Sensors Based on Lead-Free $NaNbO_3$ Piezoelectric Nanofibers. *Sensors* **2016**, *16*, 883.
(11) Koruza, J.; Groszewicz, P.; Breitzke, H.; Buntkowsky, G.; Rojac, T.; Malič, B. Grain-Size-Induced Ferroelectricity in $NaNbO_3$. *Acta Mater.* **2017**, *126* (57), 77–85.
(12) Singh, S.; Khare, N. Electrically Tuned Photoelectrochemical Properties of Ferroelectric Nanostructure $NaNbO_3$ Films. *Appl. Phys. Lett.* **2017**, *110* (15), 152902.
(13) Chao, L.; Hou, Y.; Zheng, M.; Yue, Y.; Zhu, M. Macroscopic Ferroelectricity and Piezoelectricity in Nanostructured $NaNbO_3$ Ceramics. *Appl. Phys. Lett.* **2017**, *110*, 122901.
(14) Li, P.; Ouyang, S.; Xi, G.; Kako, T.; Ye, J. The Effects of Crystal Structure and Electronic Structure on Photocatalytic H_2 Evolution and CO_2 Reduction over Two Phases of Perovskite-Structured $NaNbO_3$. *J. Phys. Chem. C* **2012**, *116*, 7621–7628.
(15) Li, P.; Ouyang, S.; Zhang, Y.; Kako, T.; Ye, J. Surface-Coordination-Induced Selective Synthesis of Cubic and Orthorhombic $NaNbO_3$ and Their Photocatalytic Properties. *J. Mater. Chem. A* **2013**, *1* (4), 1185–1191.
(16) Gu, Q.; Zhu, K.; Zhang, N.; Sun, Q.; Liu, P.; Liu, J.; Wang, J.; Li, Z. Modified Solvothermal Strategy for Straightforward Synthesis of Cubic $NaNbO_3$ Nanowires with Enhanced Photocatalytic H_2 Evolution. *J. Phys. Chem. C* **2015**, *119* (46), 25956–25964.
(17) Opoku, F.; Govender, K. K.; van Sittert, C. G. C. E.; Govender, P. P. Tuning the Electronic Structures, Work Functions, Optical Property and Stability of Bifunctional Hybrid Graphene Oxide/V–doped $NaNbO_3$ type–II Heterostructures: A Promising Photocatalyst for H_2 production. *Carbon* **2018**, *136*, 187–195.
(18) Zeng, S.; Kar, P.; Thakur, U. K.; Shankar, K. A Review on Photocatalytic CO_2 reduction Using Perovskite Oxide Nanomaterials. *Nanotechnology* **2018**, *29*, 052001.
(19) Lais, A.; Gondal, M. A.; Dastageer, M. A. Semiconducting Oxide Photocatalysts for Reduction of CO_2 to Methanol. *Environ. Chem. Lett.* **2018**, *16* (1), 183–210.
(20) Yu, Q.; Zhang, F.; Li, G.; Zhang, W. Preparation and Photocatalytic Activity of Triangular Pyramid $NaNbO_3$. *Appl. Catal. B Environ.* **2016**, *199*, 166–169.
(21) Wang, G. Z.; Chen, H.; Wu, G.; Kuang, A. L.; Yuan, H. K. Hybrid Density Functional Study on Mono- and Codoped $NaNbO_3$ for Visible-Light Photocatalysis. *ChemPhysChem* **2016**, *17*, 489–499.
(22) Xu, J.; Feng, B.; Wang, Y.; Qi, Y.; Niu, J.; Chen, M. BiOCl Decorated $NaNbO_3$ Nanocubes: A Novel p-n Heterojunction Photocatalyst With Improved Activity for Ofloxacin Degradation. *Front. Chem.* **2018**, *6*, 1–9.
(23) Chen, W.; Hu, Y.; Ba, M. Surface Interaction between Cubic Phase $NaNbO_3$ nanoflowers and Ru Nanoparticles for Enhancing Visible-Light Driven Photosensitized Photocatalysis. *Appl. Surf. Sci.* **2018**, *435*, 483–493.
(24) Glazer, A. M.; Megaw, H. D. Studies of the Lattice Parameters and Domains in the Phase Transitions of $NaNbO_3$. *Acta Crystallogr. Sect. A* **1973**, *29* (5), 489–495.
(25) Mishra, S. K.; Mittal, R.; Pomjakushin, V. Y.; Chaplot, S. L. Phase Stability and Structural Temperature Dependence in Sodium Niobate: A High-Resolution Powder Neutron Diffraction Study. *Phys. Rev. B* **2011**, *83* (13), 134105.
(26) Peel, M. D.; Thompson, S. P.; Daoud-Aladine, A.; Ashbrook, S. E.; Lightfoot, P. New Twists on the Perovskite Theme: Crystal Structures of the Elusive Phases R and S of $NaNbO_3$. *Inorg. Chem.* **2012**, *51* (12), 6876–6889.
(27) Bondarev, V. S.; Kartashev, A. V; Gorev, M. V; Flerov, I. N.; Pogorel'tsev, E. I.; Molokeev, M. S.; Raevskaya, S. I.; Suzdalev, D. V; Raevskii, I. P. Thermal and Physical Properties of Sodium Niobate Ceramics over a Wide Temperature Range. *Phys. Solid State* **2013**, *55* (4), 821–828.
(28) Shigemi, A.; Wada, T. Enthalpy of Formation of Various Phases and Formation Energy of Point Defects in Perovskite-Type $NaNbO_3$ by First-Principles Calculation. *Jpn. J. Appl. Phys.* **2004**, *43* (9B), 6793–6798.

(29) Fritsch, D. Electronic and Optical Properties of Sodium Niobate: A Density Functional Theory Study. *Adv. Mater. Sci. Eng.* **2018**, *2018*, 10–12.

(30) Johnston, K. E.; Tang, C. C.; Parker, J. E.; Knight, K. S.; Lightfoot, P.; Ashbrook, S. E. The Polar Phase of $NaNbO_3$: A Combined Study by Powder Diffraction, Solid-State NMR , and First-Principles Calculations. *J. Am. Chem. Soc.* **2010**, *132* (25), 8732–8746.

(31) Goldschmidt, V. M. Crystal Structure and Chemical Constitution. *Trans. Faraday Soc.* **1929**, 253–283.

(32) Shannon, R. D. Revised Effective Ionic Radii and Systematic Studies of Interatomic Distances in Halides and Chalcogenides. *Acta Crystallogr. Sect. A* **1976**, *32*, 751–767.

(33) Sakowski-Cowley, A. C.; Łukaszewicz, K.; Megaw, H. D. The Structure of Sodium Niobate at Room Temperature, and the Problem of Reliability in Pseudosymmetric Structures. *Acta Crystallogr. Sect. B Struct. Crystallogr. Cryst. Chem.* **1969**, *25* (5), 851–865.

(34) Shuvaeva, V. A.; Antipin, M. Y.; Lindeman, R. S. V.; Fesenko, O. E.; Smotrakov, V. G.; Struchkov, Y. T. Crystal Structure of the Electric-Fieldinduced Ferroelectric Phase of $NaNbO_3$. *Ferroelectrics* **1993**, *141* (1), 307–311.

(35) Shiratori, Y.; Magrez, A.; Fischer, W.; Pithan, C.; Waser, R.; Ju, D.-. Polymorphism in Micro- , Submicro- , and Nanocrystalline $NaNbO_3$. *J. Phys. Chem. C* **2005**, *109*, 20122–20130.

(36) Shiratori, Y.; Magrez, A.; Fischer, W.; Pithan, C.; Waser, R. Temperature-Induced Phase Transitions in Micro-, Submicro-, and Nanocrystalline $NaNbO_3$. *J. Phys. Chem. B* **2007**, *111*, 18493–18502.

(37) Darlington, C. N. W.; Knight, K. S. On the Lattice Parameters of Sodium Niobate at Room Temperature and Above. *Phys. B Condens. Matter* **1999**, *266* (4), 368–372.

(38) Petrícek, V.; Dušek, M.; Palatinus, L. Crystallographic Computing System JANA2006: General Features. *Zeitschrift fur Krist.* **2014**, *229* (5), 345–352.

(39) Massiot, D.; Fayon, F.; Capron, M.; King, I.; Le Calvé, S.; Alonso, B.; Durand, J.-O.; Bujoli, B.; Gan, Z.; Hoatson, G. Modelling One- and Two-Dimensional Solid-State NMR Spectra. *Magn. Reson. Chem.* **2002**, *40* (1), 70–76.

(40) Ewald, P. P. Die Berechnung Optischer Und Elektrostatischer Gitterpotentiale. *Ann. Phys.* **1921**, *369* (3), 253–287.

(41) Kresse, G.; Hafner, J. Ab Initio Molecular Dynamics for Liquid Metals. *Phys. Rev. B* **1993**, *47* (1), 558–561.

(42) Kresse, G.; Furthmüller, J. Efficiency of Ab-Initio Total Energy Calculations for Metals and Semiconductors Using a Plane-Wave Basis Set. *Comput. Mater. Sci.* **1996**, *6* (1), 15–50.

(43) Blöchl, P. E. Projector Augmented-Wave Method. *Phys. Rev. B* **1994**, *50* (24), 17953–17979.

(44) Perdew, J. P.; Burke, K.; Ernzerhof, M. Generalized Gradient Approximation Made Simple. *Phys. Rev. Lett.* **1996**, *77* (18), 3865–3868.

(45) Heyd, J.; Scuseria, G. E.; Ernzerhof, M. Hybrid Functionals Based on a Screened Coulomb Potential. *J. Chem. Phys.* **2003**, *118* (18), 8207–8215.

(46) Krukau, A. V.; Vydrov, O. A.; Izmaylov, A. F.; Scuseria, G. E. Influence of the Exchange Screening Parameter on the Performance of Screened Hybrid Functionals. *J. Chem. Phys.* **2006**, *125* (22), 224106.

(47) Lacroix, P. G.; Malfant, I.; Real, J.-A.; Rodriguez, V. From Magnetic to Nonlinear Optical Switches in Spin-Crossover Complexes. *Eur. J. Inorg. Chem.* **2013**, *2013* (5–6), 615–627.

(48) Kurtz, S. K.; Perry, T. T. A Powder Technique for the Evaluation of Nonlinear Optical Materials. *J. Appl. Phys.* **1968**, *39* (8), 3798–3813.

(49) Kim, Y. M.; Reardon, D. E.; Bray, P. J. ESR Studies of Radiation-Induced Niobium Centers in Nb_2O_5-Na_2O-SiO_2 Glasses. *J. Chem. Phys.* **1968**, *48* (8), 3396–3402.

(50) Sweeney, K. L.; Halliburton, L. E. Oxygen vacancies in lithium niobate. *Appl. Phys. Lett.* **1983**, *43* (4), 336–338.

(51) Xu, H.; Su, Y.; Balmer, M. Lou; Navrotsky, A. A New Series of Oxygen-Deficient Perovskites in the $NaTi_xNb_{1-x}O_{3-0.5x}$ System: Synthesis, Crystal Chemistry, and Energetics. *Chem. Mater.* **2003**, *15* (9), 1872–1878.